Electronic Supplementary Material (ESI) for Journal of Materials Chemistry A.

Supporting information for:

Zwitterionic hydrogen-bonded organic framework (ZHOF): A metal-free water oxidation proton relay in alkaline and neutral media

Experimental

Materials and instrumentation

Graphite paper (GP), $C_{18}H_{32}N_4O_8{\cdot}4HCl{\cdot}xH_2O$ (H_4TATA), $NiCl_2.6H_2O$, (CH3)2SO (DMSO), $CH_3CN(CH_3)_2$ (DMAc), CH_3COOH (HAc), H_2SO_4, H_3PO_4 and chemical reagents were of analytical grade and used without further purification. Electrochemical tests were done with an Autolab (Eco Chemie BV, Netherlands) with NOVA software (Version 1.10) in a three-electrode cell including of a Pt wire as a counter, an Ag/AgCl (3 M KCl) as a reference and ZHOF as a working electrode in KOH and PBS electrolyte. The morphology composite was characterized by Field Emission Scanning Electron Microscopes (FE-SEM), EDS and EDS mapping. The crystallographic information of the electrode was investigated by using single-crystal X-ray diffraction (SXRD, Mar 345 dtb). Powder X-Ray Diffraction Spectrometer (PXRD) (PXRD, Rigaku-Ultima IV, Japan) was applied over a 2θ range from 20° to 80° to exhibit the structure of crystallinity. High-resolution transmission electron microscopy (HRTEM) images were evaluated on an FEI Titan Tecnai G2 F20 Super-Twin. Thermo-gravimetric Analysis (TGA) curve was performed by a thermogravimetric-differential thermal synchronization analyzer (TG 209F3 NETZSCH, Germany) at a heating rate of 20°C min-1. Brunauer–Emmett–Teller (BET) surface area and pore size were calculated by Nitrogen adsorption/desorption measurements 77 K in an automated surface area and porosity analyzer (BELSORP-mini II, Japan).

Fabrication of FGF/ZHOF

The FGF was ready via the oxidation of GF using the modified chemical method. First, a piece GF (2 cm *2 cm) was cut and immersed in a mixture of concentrated H_3PO_4 (1 mL) and H_2SO_4 (1 mL) and stirred for 1 hour[1]. Thereafter, the FGP was washed with DI water several times and finally for 2 h drying in a vacuum oven at 60 °C. Then, 0.06 g (0.139 mmol) TATA was dissolved into 16 mL DMAc: DMSO (1:1, v/v), and 4 mL HOAc (6.0 M) was slowly added into the mixture under stirring at 25 °C. The reaction mixture and a piece of FGP were transferred to the Teflon-lined stainless-steel autoclave to conduct a solvothermal reaction at 120 oC for 72 h. Finally, the reaction mixture cooled slowly in three steps (during 48 h) to reach room temperature[2]. A crystalline precipitate formed at the end of the Teflon container and at FGF. Eventually, it was washed with DI water and acetone multiple times and subsequently dried at 40 °C for use.

Computational studies

The quantum mechanical (QM) methods were applied for the optimization of the discussed structures. The interpretation of the results is based on the best results of the DFT method optimization and minimization of the structures. The DFT-B3LYP/6-31G* method was performed by the Spartan'16 package. The structures were optimized on the basis of the X-ray crystallography information. With a good agreement.

Electrochemical measurements

Electrochemical tests were done with an Autolab (Eco Chemie BV, Netherlands) with NOVA software (Version 1.11) in a three-electrode cell including of a Pt wire as a counter, an Ag/AgCl (3.0 M KCl) as a reference and the as-prepared electrodes based on the flexible graphite foil as a working electrode in KOH solution electrolyte. All the measured potentials were converted to RHE, ERHE = EAg/Agcl + 0.059 pH + 0.198 V. To evaluate the OER activities of the as-prepared catalyst, the steady state voltammograms were recorded at a scan rate of 5 mV s^{-1}. Electrochemical impedance spectroscopy (EIS) was performed by applying an alternating current voltage with 5 mV amplitude in frequency ranges of 0.01 Hz–100 kHz.

X-ray Crystallographic Study

Data collection was performed on a Rigaku Mercury CCD diffractometer with graphite-monochromated Mo-Kα (λ = 0.71073 Å) radiation at room temperature. The structures were solved by direct methods and refined by the full-matrix least-squares on F2 using the SHELXTL-97 program All non-hydrogen atoms were refined with anisotropic displacement parameters. The positions of hydrogen atoms attached to carbon atoms were generated geometrically. Attempts to locate and model the highly disordered solvent molecules in the pores were unsuccessful. Therefore, the SQUEEZE routing of PLATON was used to remove the diffraction contribution from these solvents to produce a set of solvent-free diffraction intensities[3]. Crystallographic data and structure determination summaries are listed in Table S1. The selected bond lengths and angles are listed in Tables S2 and S3 in SI. CCDC-2209418 contains the crystallographic data for this paper. Copies of these data can be obtained free of charge from The Cambridge Crystallographic Data Centre via www.ccdc.cam.ac.uk/data_request/cif.

TGA and BET Study

The Results of TGA are displayed in Figure S11. The weight of HOF slowly decreased with the increased temperature, which was caused by the breakdown of the structure of HOF and its organic group exhibited three mass-loss events. The first weight loss of 1.34% happened at 78.4°C, relevant to the volatilization of the bound water. At 234.1 ºC, the second weight loss phase starts, which a weight loss of 25.27% because of the decomposition of the -COOH groups, and dehydration. The major mass loss was emerged related to the destruction of the framework was observed after 292 °C because of the whole decomposition of HOF. This weight loss during this temperature range is roughly 67.63%, which approves high thermal stability. Results of nitrogen adsorption/desorption measurements at 77 K quoted a type II isotherm with (C=11.046) relatively low adsorption (Figure S12). The Brunauer−Emmett−Teller (BET) surface area was calculated to be 33.034 $m^2 g^{-1}$ with the pore size calculated lower than 2 nm, indicating the non-reticular framework with a small surface area.

Further charge storage characterization

The CV profiles of FGF/ZHOF at different scan rates ranging from 0.05 to 0.4 V s^{-1} show similar quasi-rectangular shapes Figure S13A. It can be seen that the quasi-rectangular shape of the CV curves is well kept at different scan rates, even at 0.4 V s^{-1}, referring to reversibility and favorable rate performance of the electrode, easy ion transport within the porous channels, and ideal double-layer capacitive feature. The rectangular-like shapes of the CV curves are the same as that of FGF/ZHOF in three electrodes system. Furthermore, the peak and area current of the CV curves increase with the increasing scan rate, due to the rate of ionic mobility being quicker, which is a function of the used potential[4]. Even the CV curves at high scan rates remain undistorted mentioning the low contact resistance of FGF/ZHOF. It is observed that FGF/ZHOF electrodes have a large surrounding CV area. The Csp of FGF/ZHOF was calculated from CV curves using equation S1[5] and the equivalent results are presented in Figure S13B.

$$C_{cv} = \frac{\int V \times dv}{\Delta V \times m \times v}$$ Equation. S1

The C_{cv} signifies the capacitance estimated according to CV curves, ΔV(V) represents window potential, ∫Vdv represents the integral area of the CV curve, v (V s^{-1}) symbolizes the scan rate, and m (g) assigned the material weight covered on the surface FGP. Furthermore, the C_{sp} of the electrode decreases as the scan rate increases, which could be attributed to the unfinished

interfacial electrode/electrolyte reactions, and reduced ion transport. The excellent electrochemical performance of FGF/ZHOF is related to the ion transport and efficient electron paths by charged orientation on the inner wall of the semi-laminated channels and the synergies effect between the pure FGF paper and FGF/ZHOF. The integrated area under the CV curve shows that the total stored charge is obtained from a faradaic portion of ion intercalation or non-Faradaic charge storage mechanisms. Trasatti analysis is applied to quantify the diffusion-controlled process, the capacitive charge storage and the portion of surface capacitance and diffusion in the electrochemical reaction process. The electrochemical reaction process was estimated by Equations [6]:

$$q_{\upsilon} = q_{cap} + \frac{\alpha}{\upsilon^{1/2}} \qquad \text{Equation. S2}$$

$$\frac{1}{q_{\upsilon}} = \frac{1}{q_{tot}} + \alpha\left(\upsilon^{\frac{1}{2}}\right) \qquad \text{Equation. S3}$$

Here, q_{υ} is estimated from the area integral under the CV curve, q_{tot} and q_{cap} signify the total charge storage and the capacitive charge storage (covering the EDLs and PCs) of the electrode, respectively. The term α ($\upsilon^{1/2}$) is the charge storage of the diffusion-controlled process, where υ is the scan rate and α is a constant. Theoretically, the diffusion-controlled charge storage process depends on the scan rate meanwhile the charge storage originating from the surface process (fast kinetics) is scan-rate independent. When the scan rate is enough high, rather of the diffusion-controlled process can be deprived of the q_{tot}. Therefore, q_{tot} and q_{cap} can be calculated by extrapolating the trend lines of the $1/q_{\upsilon}$ versus $^{1/2}$ plot to =0 and the q_{υ} versus $^{1/2}$ plot to = ∞ respectively[6,7] (see Figure S14A and B). The q_{cap} and q_{tot} were found to be 15.94 and 140.84 Cg^{-1} respectively, and the q_{diff} is 124.89 Cg^{-1} ($q_{tot} = q_{cap} + q_{diff}$). The q_v versus $v^{-1/2}$ and $1/q^{\upsilon}$ versus $v^{1/2}$ plots were also studied by the Trasatti analysis. Obviously, 88.67% of the total charge storage is presented by the diffusion charge storage (q_{diff}), confirming that the main part of the charge storage process is governed by the non-Faradaic events. To show the merit of FGF/ZHOF as an efficient electrode in SC construction, a comparison of the capacitive performances are summarized in Table S1.

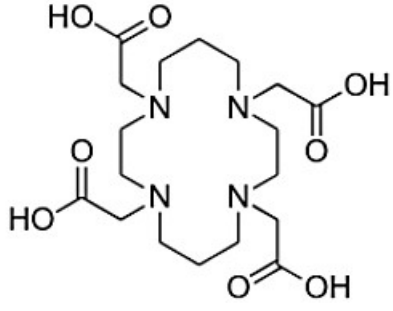

Scheme S1. The chemical structure of 1, 4, 8, 11-Tetraazacyclotetradecane-1, 4, 8, 11-tetraacetic acid.

Figure S1. The optical images taken by an optical microscope from the as-prepared ZHOF on the FGF surface

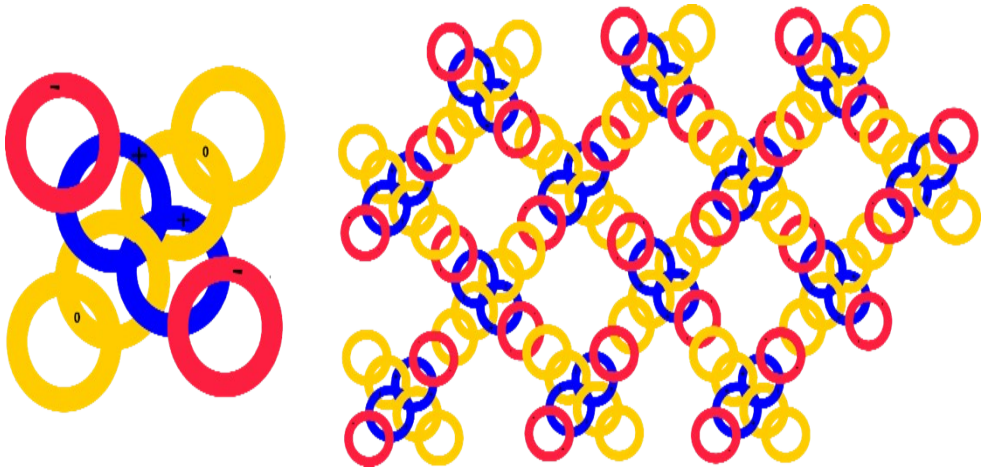

Figure S2. Schematically representation of charged separated structure of TATA, introducing a molecular synthon for the facile 2D assembling. The red circles nominate carboxylate anions, the blue circles nominate positive ammonium cations, and the yellow circles show uncharged carboxyl and amine groups.

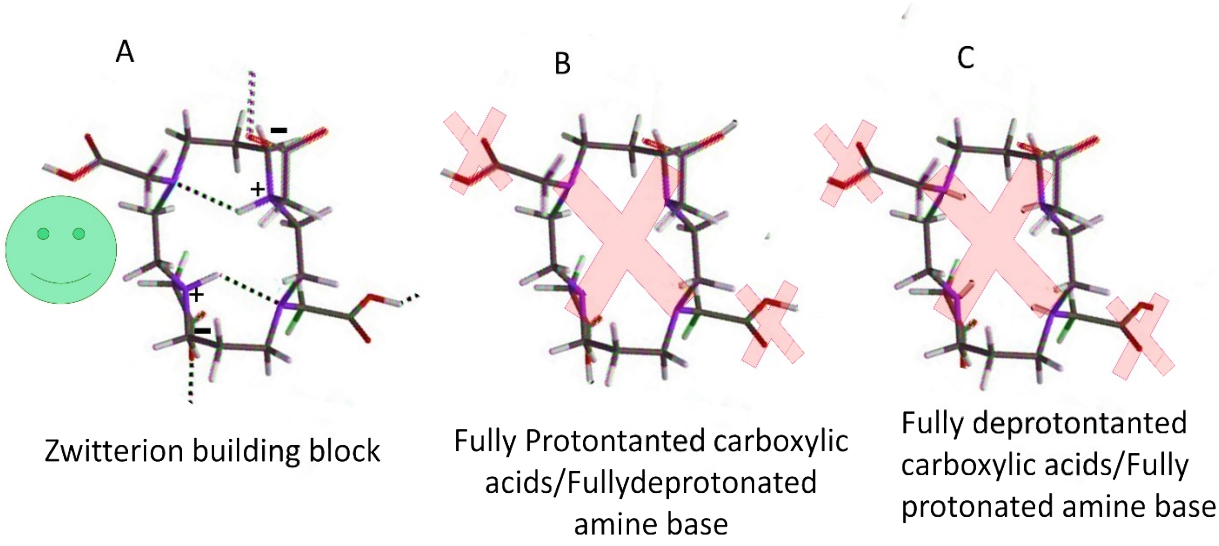

Figure S3. The Visualization of intramolecular proton allotment (intrinsic zwitterionic tectons), in which except for the zwitterionic form (left), neither one can participate in intermolecular and intramolecular H-bonding.

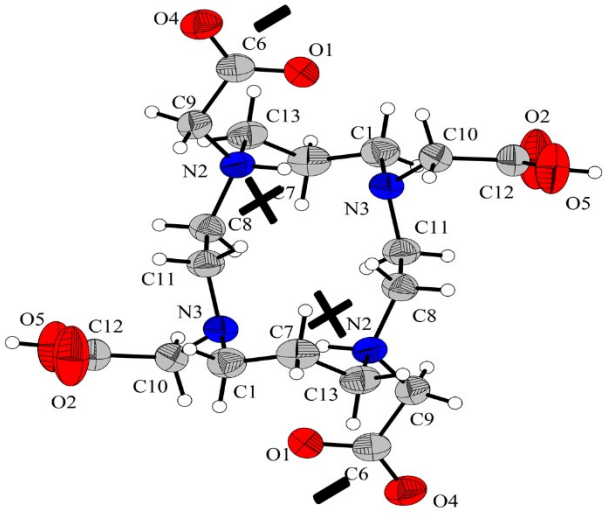

Figure S4. The ORTEP plots of the X-ray crystal structure of TATA molecules, revealing the zwitterionic sites on the skeletons. Thermal ellipsoids are drawn at a 50% probability.

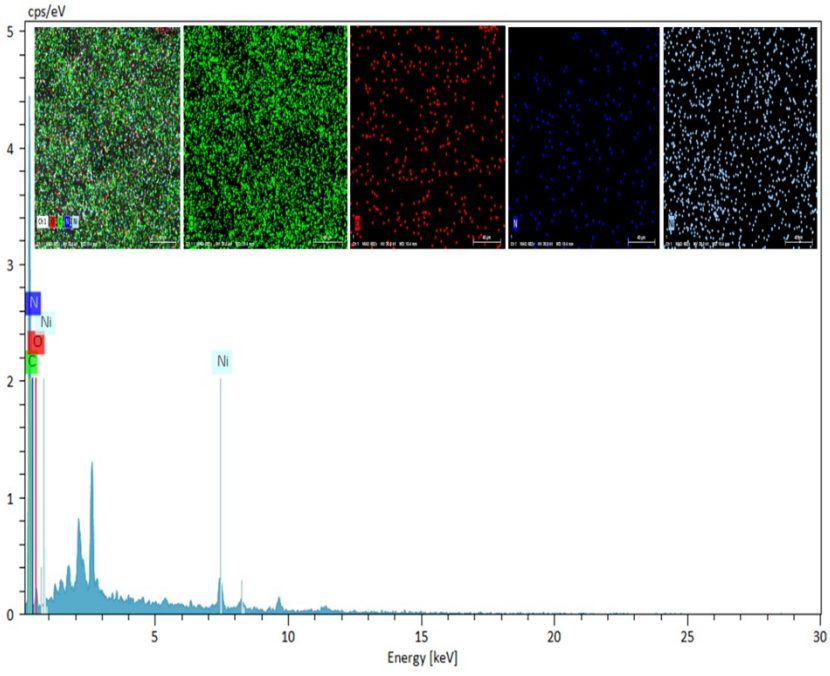

Figure S5. EDS mapping and EDX analysis FGF/ZHOF@Ni(II) electrode.

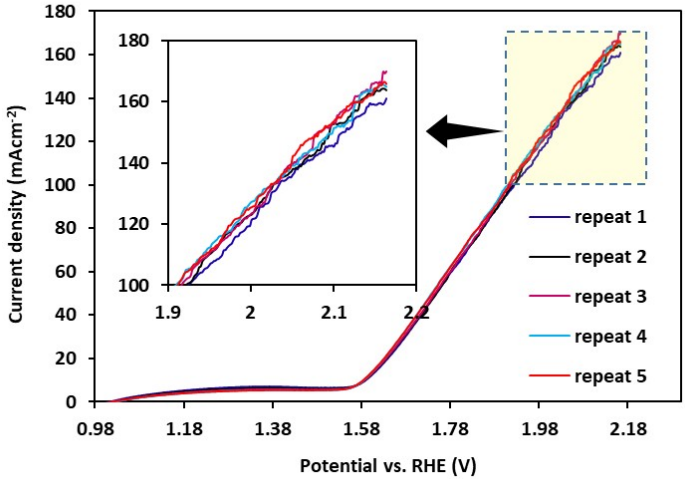

Figure S6. The repeatability of FGF/ZHOF@Ni(II) electrode in 0.1 M of KOH.

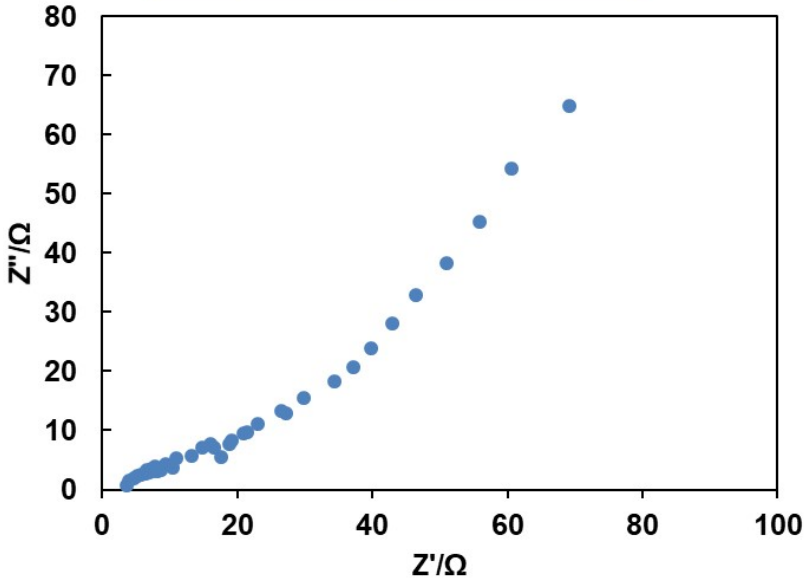

Figure S7. Electrochemical impedance spectra (EIS) of FGF/ZHOF in 0.1 M KCl containing 10 mM of $Fe(CN)_6^{3-/4-}$ under open circuit potential.

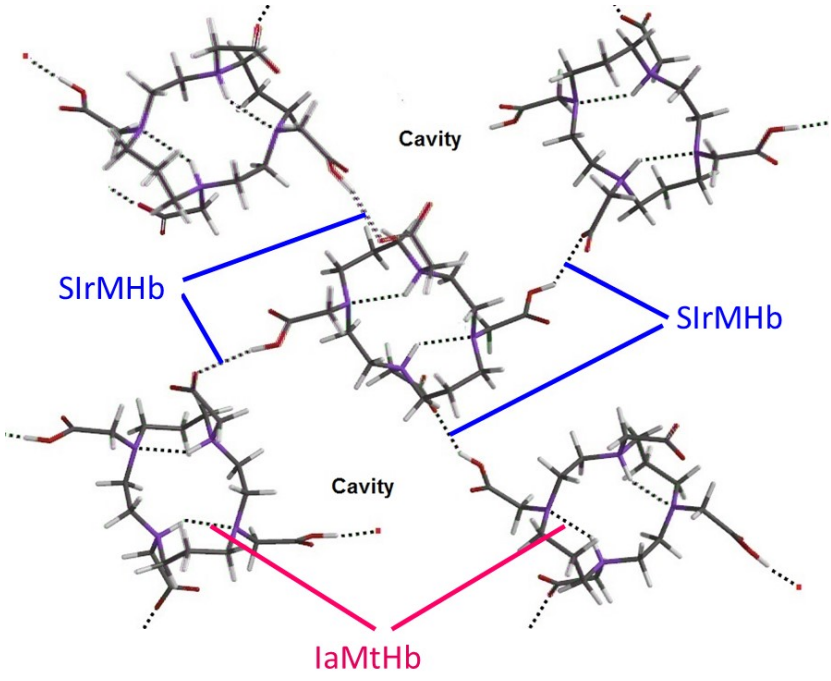

Figure S8. The optimized structure of trans-TE_2A based on X-ray crystallography by DFT-B_3LYP/6-31G*. The H-bonds, the rings and cavities among the molecular units was shown as well.

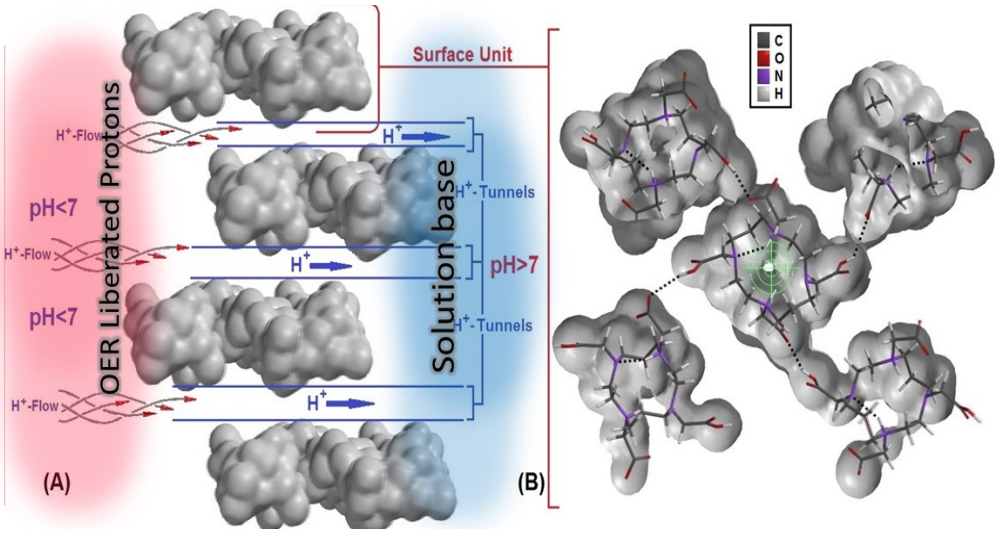

Figure S9. The density of electron of the optimized structure of trans-TATA on the basis of X-ray crystallography by DFT-B3LYP/6-31G*. (A) The layers of the trans-TATA (surface layer) and the tunnels for H^+ transfer between the layers. The local pH at the right side is assumed to be lower than 7 and the pH at the left side is upper than 7 (solution base). The H^+ flow was shown as well. (B) The layer of molecular units of trans-TATA, which they were connected by H-bonds.

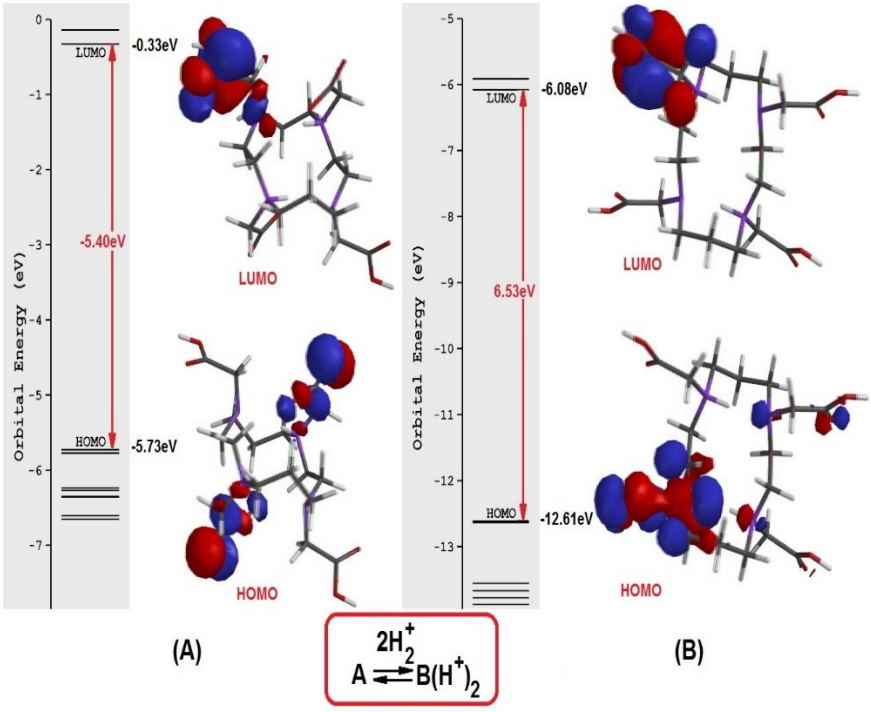

Figure S10. The HOMO and LUMO energy levels and ΔEHOMO-LUMO (in eV) energy gaps of trans-TATA, before $2H^+$ attraction (A), and after attraction $2H^+$ process (B). The calculations demonstrated that structure-A trans-TATA is a soft base than trans-TATA-$2H^+$.

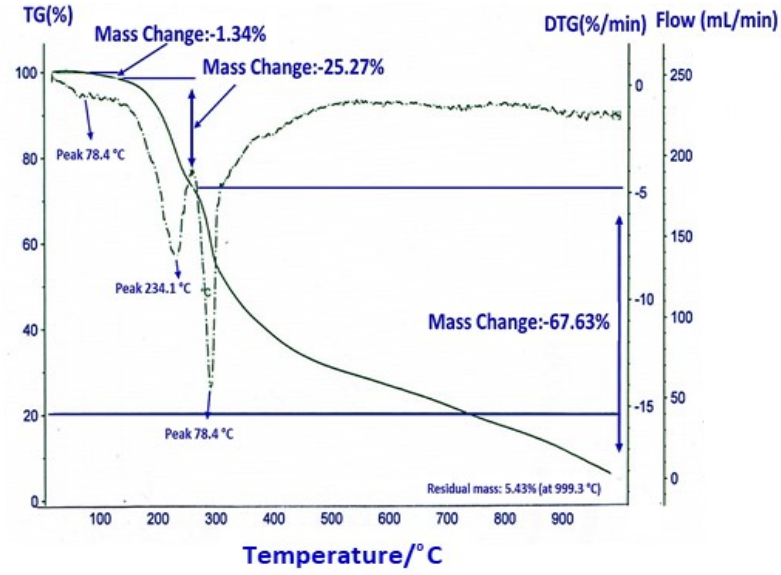

Figure S11. The TGA curves of ZHOF from 25 to 1000 °C.

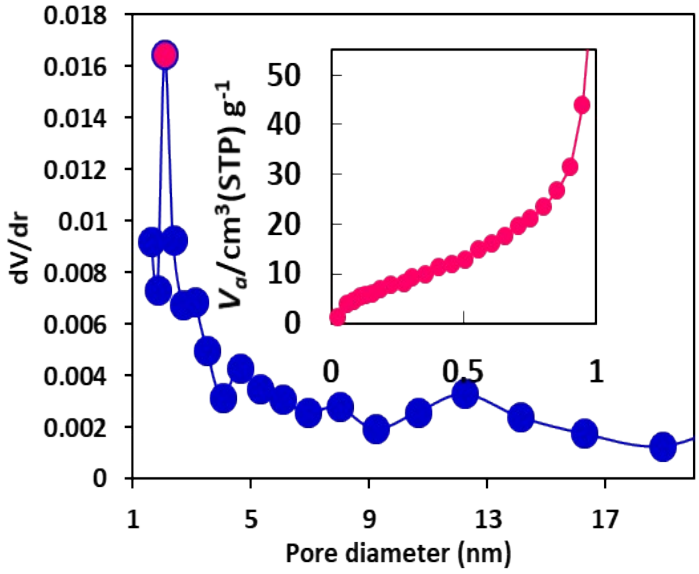

Figure S12. BET plot for Nitrogen sorption isotherms and their related pore size distribution of ZHOF.

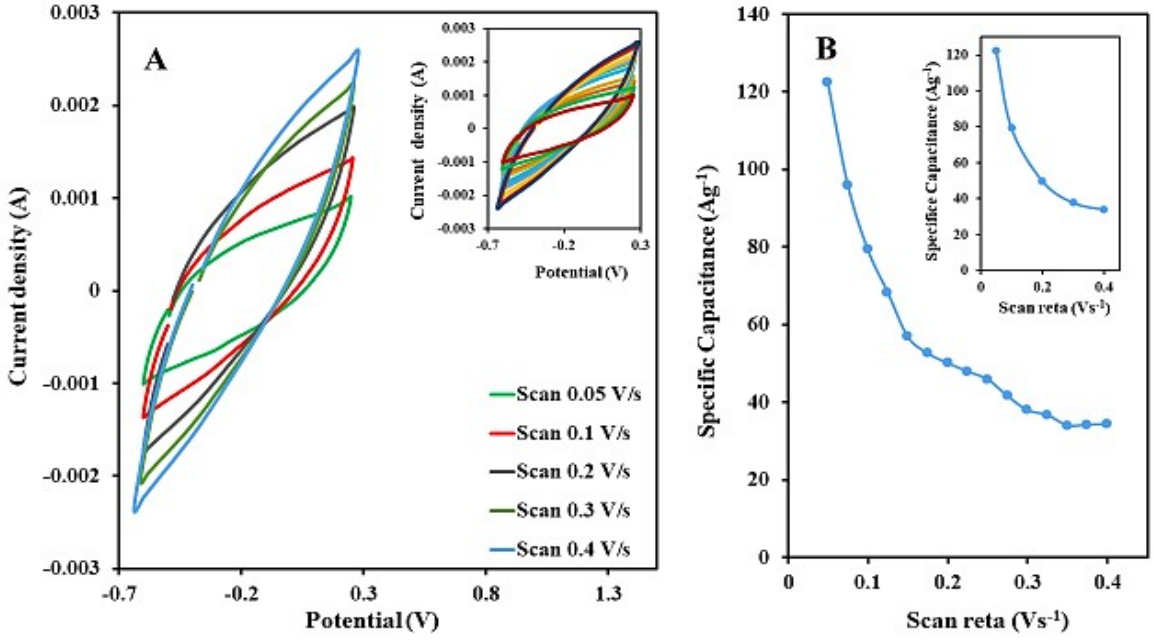

Figure S13. (A) CV curves of the FGF/ZHOF electrode at different scan rate ranging from 0.05 to 0.4 V s^{-1}, (B) Calculated capacitance as a function of scan rates for in 0.1 M KOH solution.

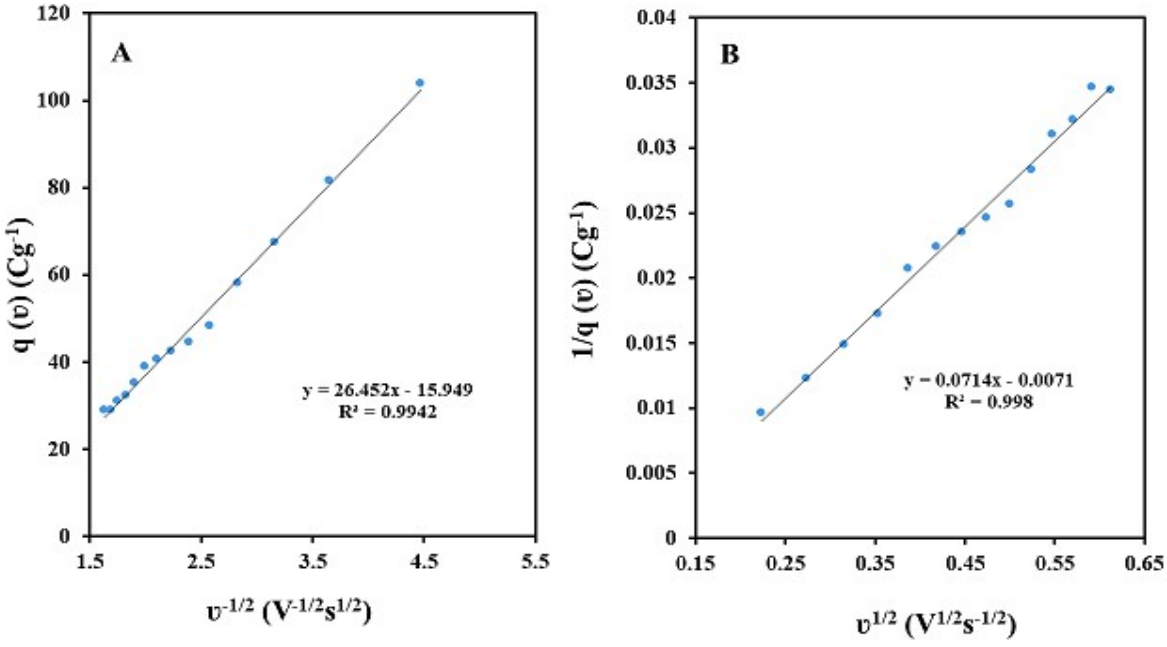

Figure S14. Trasatti analysis results based on the voltammetric charge of the FGF/ZHOF electrode (A) Extrapolating the trend line of the q(v) versus $v^{-1/2}$ plot to v= ∞ gives the q_{cap}. (B) Extrapolating the trend line of the $1/q_v$ vs. $v^{1/2}$ plot to v=0 gives the q_{tota} in 0.1 M KOH solution electrolyte.

Supplementary note:

A deep insight into the Gerischer model may be obtained by studying the TLM modified from the natural diffusion. The term of natural diffusion can be expressed by a Rs–CPE Warburg/TLM model (Figure S15). Rdiff and CPE express the transport and electro-/chemical storage processes, respectively. Thus, $(RsCp)^{-1}$ is the diffusion coefficient, D, of the Fick's law[8] .

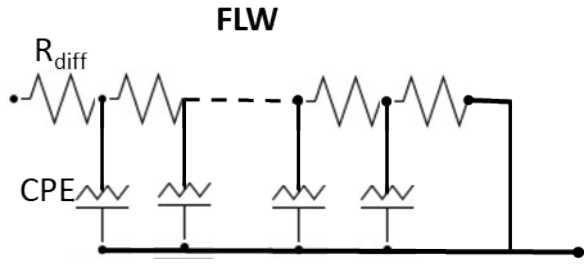

Figure S15. The representation of FLW impedance.

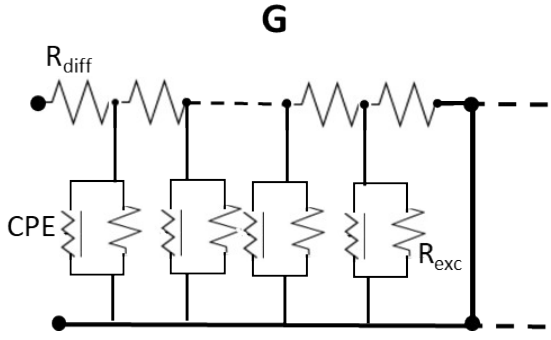

Figure S16. The Gerischer element is produced through adding Rexc in transverse direction to FLW

Despite the fact that both models disclose a semi-infinite diffusion at high frequencies, their dispersions are distinctly different in the low-frequency regions[9] where the G element being obviously depressed relevant to FLW. In high frequency part, the pure G illustrates a 45° transmission line simplified from the cotangent relation developed for the general cases of TLM[10,11]:

$$Z(\omega) = \sqrt{\frac{R_{exc}R_{diff}}{1 + i\omega\tau_G}} \qquad \text{Equation. S4}$$

Rdiff and Rexc define the diffusion resistance and exchange (chemical) resistance at the HOF/electrolyte interface. ω and τG nominate the angular frequency and 1/k (k is the rate of the chemical reaction). In Equation. S5 the product of Rs and Rex is expressed as RG, though they cannot be determined separately[12]. Further simplification of Equation. S5 reduces it to a quite simple and more applicable form,54 based on Equation. S5:

$$Z_w = Z_0[k + j]\omega^{-\frac{1}{2}} \qquad \text{Equation. S5}$$

The peak frequency (τG) of the asymmetric arc of G is equivalent to $\sqrt{3}\tau_G$. Hence, we can evaluate rate of exchange reaction (k).

Emerging FLW shows that the rate of exchange reaction is lower or comparable with the natural diffusion (Rex < Rdiff), while in the case of Gerischer impedance, rate of diffusion is extremely lagged from the rate of exchange reaction (Rex<<Rdiff). Indeed, observing the G impedance implies a practically blocked natural diffusion at FGF/ZHOF, in which the released protons are efficiently shuttled through the micrpourous crystalline channels. The equation S6 defines the pure (normal) Gerischer, as distinct ideal case that frequently has been demonstrated to distinguish it from depressed Gerischer, an actual case representing deviations from the pure G. The main deviation of the pure G is attributed to an experimental Nyquist plot exhibiting a slope lower than 45° at high frequency region. This behavior has been indexed by the 'fractal Gerischer' or 'depressed Gerischer', defined by:

$$Z_w = Z_0[k + j]\omega^{-n} \qquad \text{Equation. S6}$$

For the n values ranged on 0 to 0.5, we have a significant depression in the impedance arc in Nyquist diagram. When n→0.5, the depressed G plot coincides with the pure G (identified by a 45° straight line in high frequencies). As in the case of CPE/Cdl, the deviation from pure G has been related to time constant dispersion originated from surface roughness and the structural inhomogeneities, the Fractal behavior[13–15].

$$Z_G\sqrt{\frac{z}{y}} = \sqrt{\frac{R_s}{R_P^{-1} + i\omega C_P}} \qquad \text{Equation. S7}$$

This model can describe accompanying diffusion and reaction process of the equation, where, the reaction constant k corresponds to (RpCp)−1 [16].

$$\frac{\partial C(x,t)}{\partial t} = D\frac{\partial^2 C(x,t)}{\partial X^2} + k(c(x,t<0) - c(x,t)) \qquad \text{Equation. S8}$$

The extra Rp in Gerischer model then represents the co-existing exchange reaction during the diffusion, which plays a role of a 'sink' of the transport species. Therefore, the proper analysis of the Gerischer function can provide both the diffusion and reaction kinetics for the processes occurring within the quasi-homogeneous medium including the porous structure. The situation should be distinguished from the case where the reaction is concerned with the in/excorporation at the sample boundary only and the governing equation is the conventional Fick's equation, Equation. S5 for the Warburg impedance.

Table S1. Electrochemical performance of the organic framework based- supercapacitors.

Electrode Materials	Potential Window (V)	SC at 1 Ag-1 (Fg-1)	Power density (Wkg-1)	Energy density (Whkg-1)	Cyclic stability	Electrolyte	Ref.
PDC–MA–COF//AC	0 to 1.5	94	750	29.2	88% (20000)	6 M KOH	[17]
CTFs	0 to 0.8	379	975	46.3	96.8% (10000)	1 M H_2SO_4	[18]
S@Ni-MOF//AC	0 to 1.6	136.5	800	48.54	86.67 % (20000)	3 M KOH	[19]
GNPC-0.75	0 to 1.2	420	304	21.1	85 % (60000)	1 M H_2SO_4	[20]
PANI/UiO-669	0 to 0.8	1015	200	78.8	91% (5000)	1 M H_2SO_4	[21]
PTF-700	0 to 3.5	151.3	7500	47.4	85% (10000)	$EMIMBF_4$	[22]
FGF/ZHOF	-0.6 to .25	903.41	425	90.65	113% (10000)	0.1 M KOH	-

Table S2. Crystal data and refinement parameters of the ZHOF crystal.

Chemical formula	*C18H32N4O8*
Mr	*432.47*
Crystal system, space group	*Monoclinic, $P2_1/n$*
Temperature (K)	*290*
a, b, c (Å)	*7.7598 (16), 15.946 (3), 8.3038 (17)*
β (°)	*97.56 (3)*
V ($Å^3$)	*1018.6 (4)*
Z	*2*
Radiation type	*Mo Kα*
μ (mm^{-1})	*0.11*
Crystal size (mm)	*0.2 × 0.15 × 0.1*
Data collection	
Diffractometer	*MAR345**
Absorption correction	-
No. of measured, independent and observed [I > 2σ(I)] reflections	*5209, 1724, 1256*
Rint	*0.058*
(sin θ/λ)max ($Å^{-1}$)	*0.594*
Refinement:	
$R[F^2 > 2\sigma(F^2)]$, $wR(F^2)$, S	*0.091, 0.263, 1.05*
No. of reflections	*1724*
No. of parameters	*141*
No. of restraints	*2*
H-atom treatment	*H atoms treated by a mixture of independent and constrained refinement*
Δρmax, Δρmin (e $Å^{-3}$)	*0.41, -0.35*
Primary atom site location	*structure-invariant direct methods*
Hydrogen site location:	*mixed*
H atoms treated by a mixture of independent and constrained refinement	
$w = 1/[\sigma^2(F^2) + (0.0565P)^2 + 1.5301P]$	
where $P = (F^2 + 2F^2)/3$ $(\Delta/\sigma)_{max} < 0.001$	
Radiation source: fine-focus sealed tube Mirrors monochromator	
Detector resolution: 0.81 pixels mm^{-1} image–plate detector – phi oscillation scans 6151 measured reflections	
1726 independent reflections 1482 reflections with I > 2σ(I)	
R_{int}	*0.058*
θ_{max} and θ_{min}	*25.0°, 2.6°*
h =	*−9→9*
k =	*0→18*
l =	*0→9*

Geometry*:* All e.s.d.'s (except the e.s.d. in the dihedral angle between two l.s. planes) are estimated using the full covariance matrix. The cell e.s.d.'s are taken into account individually in the estimation of e.s.d.'s in distances, angles and torsion angles; correlations between e.s.d.'s in cell parameters are only used when they are defined by crystal symmetry. An approximate (isotropic) treatment of cell e.s.d.'s is used for estimating e.s.d.'s involving l.s. planes

*Computer programs: MAR345 dtb Program (1.24-4, 2013), Automar software package (3.3a, 2015), SHELXT 2018/2 (Sheldrick, 2018), SHELXL2016/6 (Sheldrick, 2016), DIAMOND (Brandenburg, 1999), PLATON (2018). [R1, R2]

[R1] Sheldrick, G. M. (2008). Acta Cryst. A64, 112-122.

[R2] Sheldrick, G. M. (2015). Acta Cryst. C71, 3-8

Table S3. Fractional atomic coordinates and isotropic or equivalent isotropic displacement parameters (Å2*)*

	x	*y*	*z*	U_{iso}*/U_{eq}
O1	*−0.0039 (3)*	*0.57847 (17)*	*0.3608 (4)*	*0.0512 (8)*
N2	*0.2603 (4)*	*0.4875 (2)*	*0.2856 (4)*	*0.0418 (8)*
H2	*0.271641*	*0.526047*	*0.378284*	*0.050**
N3	*0.5980 (4)*	*0.3661 (2)*	*0.5466 (4)*	*0.0435 (8)*
O4	*−0.2068 (3)*	*0.48915 (19)*	*0.2503 (4)*	*0.0569 (8)*
O5	*0.6477 (5)*	*0.2171 (2)*	*0.2366 (5)*	*0.0784 (12)*
C6	*−0.0557 (5)*	*0.5102 (3)*	*0.2954 (5)*	*0.0439 (9)*
C7	*0.5860 (5)*	*0.3950 (3)*	*0.8410 (5)*	*0.0533 (11)*
H7A	*0.475224*	*0.422961*	*0.811694*	*0.064**
H7B	*0.581488*	*0.366576*	*0.943594*	*0.064**
C8	*0.4065 (5)*	*0.4258 (3)*	*0.3141 (5)*	*0.0466 (10)*
H8A	*0.515385*	*0.455059*	*0.309619*	*0.056**
H8B	*0.393351*	*0.384667*	*0.227266*	*0.056**
C9	*0.0865 (5)*	*0.4468 (3)*	*0.2764 (5)*	*0.0466 (10)*
H9A	*0.089257*	*0.404812*	*0.361298*	*0.056**
H9B	*0.060234*	*0.418565*	*0.172580*	*0.056**
C10	*0.6968 (5)*	*0.3188 (2)*	*0.4384 (5)*	*0.0458 (10)*
H10A	*0.814618*	*0.312024*	*0.492466*	*0.055**
H10B	*0.703033*	*0.352300*	*0.341807*	*0.055**
C11	*0.4159 (5)*	*0.3803 (3)*	*0.4760 (5)*	*0.0476 (10)*
H11A	*0.357577*	*0.413416*	*0.550625*	*0.057**
H11B	*0.356270*	*0.326884*	*0.460272*	*0.057**
C12	*0.6273 (5)*	*0.2333 (3)*	*0.3857 (5)*	*0.0488 (10)*
C13	*0.2718 (5)*	*0.5390 (3)*	*0.1352 (5)*	*0.0489 (10)*
H13A	*0.161073*	*0.566488*	*0.103403*	*0.059**
H13B	*0.293455*	*0.501927*	*0.047486*	*0.059**
O2	*0.5528 (6)*	*0.1873 (2)*	*0.4664 (5)*	*0.0989 (15)*
C1	*0.6090 (5)*	*0.3299 (3)*	*0.7121 (5)*	*0.0504 (10)*
H1A	*0.721192*	*0.302960*	*0.739012*	*0.060**
H1B	*0.520084*	*0.287167*	*0.712956*	*0.060**
H5	*0.602 (7)*	*0.171 (4)*	*0.208 (7)*	*0.082 (18)**

Atomic displacement parameters (Å2)

	U^{11}	U^{22}	U^{33}	U^{12}	U^{13}	U^{23}
O1	*0.0498 (16)*	*0.0469 (17)*	*0.0563 (18)*	*0.0054 (13)*	*0.0039 (13)*	*−0.0031 (14)*
N2	*0.0369 (16)*	*0.0481 (18)*	*0.0392 (18)*	*0.0031 (14)*	*0.0007 (13)*	*0.0006 (14)*
N3	*0.0367 (16)*	*0.0450 (18)*	*0.0485 (19)*	*0.0039 (14)*	*0.0040 (14)*	*0.0002 (15)*
O4	*0.0379 (16)*	*0.0662 (19)*	*0.066 (2)*	*−0.0009 (13)*	*0.0040 (13)*	*0.0039 (15)*
O5	*0.100 (3)*	*0.063 (2)*	*0.077 (2)*	*−0.031 (2)*	*0.033 (2)*	*−0.0223 (19)*
C6	*0.043 (2)*	*0.052 (2)*	*0.036 (2)*	*0.0021 (18)*	*0.0052 (16)*	*0.0091 (18)*
C7	*0.046 (2)*	*0.063 (3)*	*0.052 (3)*	*0.003 (2)*	*0.0088 (19)*	*0.013 (2)*
C8	*0.040 (2)*	*0.050 (2)*	*0.050 (2)*	*0.0068 (18)*	*0.0055 (17)*	*−0.0021 (18)*
C9	*0.039 (2)*	*0.049 (2)*	*0.051 (2)*	*0.0005 (17)*	*0.0028 (17)*	*−0.0038 (19)*
C10	*0.042 (2)*	*0.042 (2)*	*0.053 (2)*	*0.0019 (17)*	*0.0035 (17)*	*−0.0023 (18)*
C11	*0.036 (2)*	*0.050 (2)*	*0.056 (3)*	*0.0022 (17)*	*0.0027 (17)*	*0.0043 (19)*
C12	*0.049 (2)*	*0.044 (2)*	*0.053 (2)*	*−0.0015 (19)*	*0.0049 (19)*	*−0.004 (2)*
C13	*0.045 (2)*	*0.063 (3)*	*0.038 (2)*	*0.0057 (19)*	*0.0021 (17)*	*0.0063 (19)*
O2	*0.177 (4)*	*0.059 (2)*	*0.065 (2)*	*−0.043 (3)*	*0.032 (3)*	*−0.0058 (18)*

C1	*0.050 (2)*	*0.051 (2)*	*0.049 (3)*	*0.0012 (19)*	*0.0027 (19)*	*0.0101 (19)*

Geometric parameters (Å, º)

O1—C6	*1.259 (5)*	*C8—H8A*	*0.9700*
N2—H2	*0.9800*	*C8—H8B*	*0.9700*
N2—C8	*1.497 (5)*	*C8—C11*	*1.521 (6)*
N2—C9	*1.490 (5)*	*C9—H9A*	*0.9700*
N2—C13	*1.506 (5)*	*C9—H9B*	*0.9700*
N3—C10	*1.463 (5)*	*C10—H10A*	*0.9700*
N3—C11	*1.475 (5)*	*C10—H10B*	*0.9700*
N3—C1	*1.483 (5)*	*C10—C12*	*1.511 (6)*
O4—C6	*1.229 (5)*	*C11—H11A*	*0.9700*
O5—C12	*1.295 (5)*	*C11—H11B*	*0.9700*
O5—H5	*0.83 (6)*	*C12—O2*	*1.193 (5)*
C6—C9	*1.520 (5)*	*C13—H13A*	*0.9700*
C7—H7A	*0.9700*	*C13—H13B*	*0.9700*
C7—H7B	*0.9700*	*C1—H1A*	*0.9700*
C7—C13^{i}	*1.518 (6)*	*C1—H1B*	*0.9700*
C7—C1	*1.519 (6)*		
C8—N2—H2	*107.5*	*C6—C9—H9B*	*109.3*
C8—N2—C13	*111.3 (3)*	*H9A—C9—H9B*	*107.9*
C9—N2—H2	*107.5*	*N3—C10—H10A*	*108.2*
C9—N2—C8	*112.6 (3)*	*N3—C10—H10B*	*108.2*
C9—N2—C13	*110.3 (3)*	*N3—C10—C12*	*116.5 (3)*
C13—N2—H2	*107.5*	*H10A—C10—H10B*	*107.3*
C10—N3—C11	*112.8 (3)*	*C12—C10—H10A*	*108.2*
C10—N3—C1	*113.4 (3)*	*C12—C10—H10B*	*108.2*
C11—N3—C1	*111.3 (3)*	*N3—C11—C8*	*110.9 (3)*
C12—O5—H5	*111 (4)*	*N3—C11—H11A*	*109.5*
O1—C6—C9	*115.2 (3)*	*N3—C11—H11B*	*109.5*
O4—C6—O1	*127.2 (4)*	*C8—C11—H11A*	*109.5*
O4—C6—C9	*117.6 (4)*	*C8—C11—H11B*	*109.5*
H7A—C7—H7B	*107.6*	*H11A—C11—H11B*	*108.1*
C13^{i}—C7—H7A	*108.6*	*O5—C12—C10*	*111.9 (4)*
C13^{i}—C7—H7B	*108.6*	*O2—C12—O5*	*123.0 (4)*
C13^{i}—C7—C1	*114.5 (3)*	*O2—C12—C10*	*125.0 (4)*
C1—C7—H7A	*108.6*	*N2—C13—C7^{i}*	*113.0 (3)*
C1—C7—H7B	*108.6*	*N2—C13—H13A*	*109.0*
N2—C8—H8A	*108.8*	*N2—C13—H13B*	*109.0*
N2—C8—H8B	*108.8*	*C7^{i}—C13—H13A*	*109.0*
N2—C8—C11	*113.6 (3)*	*C7^{i}—C13—H13B*	*109.0*
H8A—C8—H8B	*107.7*	*H13A—C13—H13B*	*107.8*
C11—C8—H8A	*108.8*	*N3—C1—C7*	*112.9 (3)*
C11—C8—H8B	*108.8*	*N3—C1—H1A*	*109.0*
N2—C9—C6	*111.7 (3)*	*N3—C1—H1B*	*109.0*
N2—C9—H9A	*109.3*	*C7—C1—H1A*	*109.0*
N2—C9—H9B	*109.3*	*C7—C1—H1B*	*109.0*
C6—C9—H9A	*109.3*	*H1A—C1—H1B*	*107.8*
O1—C6—C9—N2	*−19.7 (5)*	*C10—N3—C11—C8*	*−57.1 (4)*

N2—C8—C11—N3	*−143.5 (3)*	*C10—N3—C1—C7*	*152.4 (3)*
N3—C10—C12—O5	*142.9 (4)*	*C11—N3—C10—C12*	*−58.1 (5)*
N3—C10—C12—O2	*−32.8 (7)*	*C11—N3—C1—C7*	*−79.1 (4)*
O4—C6—C9—N2	*162.1 (3)*	*C13—N2—C8—C11*	*172.2 (3)*
C8—N2—C9—C6	*163.9 (3)*	*C13—N2—C9—C6*	*−71.1 (4)*
C8—N2—C13—C7^{i}	*−74.4 (4)*	*C13^{i}—C7—C1—N3*	*−64.7 (4)*
C9—N2—C8—C11	*−63.4 (4)*	*C1—N3—C10—C12*	*69.6 (5)*
C9—N2—C13—C7^{i}	*159.9 (3)*	*C1—N3—C11—C8*	*174.0 (3)*

Symmetry code: (i) −*x*+1, −*y*+1, −*z*+1.

References

1 M. P. Down, S. J. Rowley-Neale, G. C. Smith and C. E. Banks, ACS Applied Energy Materials, 2018, 1, 707–714.

2 R. Wen, Y. Li, M. Zhang, X. Guo, X. Li, X. Li, J. Han, S. Hu, W. Tan, L. Ma and S. Li, Journal of Hazardous Materials, 2018, 358, 273–285.

3 A. L. Spek, Journal of Applied Crystallography, 2003, 36, 7–13.

4 K. R. Shrestha, S. Kandula, N. H. Kim and J. H. Lee, Journal of Alloys and Compounds, 2019, 771, 810–820.

5 G. Ghanashyam and H. K. Jeong, Chemical Physics Letters, 2019, 722, 39–43.

6 X. Zhou, T. Meng, F. Yi, D. Shu, D. Han, Z. Zhu, A. Gao, C. Liu, X. Li, K. Yang and H. Yi, Journal of Power Sources, 2020, 475, 228554.

7 H. Liu, H. Guo, W. Yao, L. Zhang, M. Wang, T. Fan, W. Yang and W. Yang, Colloids and Surfaces A: Physicochemical and Engineering Aspects, 2020, 601, 125011.

8 P. Costamagna, E. M. Sala, W. Zhang, M. Lund Traulsen and P. Holtappels, Electrochimica Acta, 2019, 319, 657–671.

9 M. Shamsipur, M. Ardeshiri, A. A. Taherpour and A. Pashabadi, Journal of Materials Chemistry A, 2021, 9, 2937–2947.

10 E. C. Shin, P. A. Ahn, H. H. Seo, J. M. Jo, S. D. Kim, S. K. Woo, J. H. Yu, J. Mizusaki and J. S. Lee, Solid State Ionics, 2013, 232, 80–96.

11 F. Fabregat-santiago and J. Bisquert, 2005, 87, 117–131.

12 J. Bisquert, I. Mora-Sero and F. Fabregat-Santiago, ChemElectroChem, 2014, 1, 289–296.

13 W. Zipprich, B. A. Boukamp, G. Pudmich and F. Tietz, 2001, 256–264.

14 B. A. Boukamp, M. Verbraeken, D. H. A. Blank and P. Holtappels, 2006, 177, 2539–2541.

15 B. A. Boukamp, 2004, 169, 65–73.

16 J. Bisquert, 2002, 325–333.

17 L. Li, F. Lu, R. Xue, B. Ma, Q. Li, N. Wu, H. Liu, W. Yao, H. Guo and W. Yang, ACS Applied Materials and Interfaces, 2019, 11, 26355–26363.

18 Y. Gao, C. Zhi, P. Cui, K. A. I. Zhang, L. P. Lv and Y. Wang, Chemical Engineering Journal, , DOI:10.1016/j.cej.2020.125967.

19 L. Yue, H. Guo, X. Wang, T. Sun, H. Liu, Q. Li, M. Xu, Y. Yang and W. Yang, Journal of Colloid and Interface Science, 2019, 539, 370–378.

20 X. Shi, S. Zhang, X. Chen, T. Tang and E. Mijowska, Carbon, 2020, 157, 55–63.

21 L. Shao, Q. Wang, Z. Ma, Z. Ji, X. Wang, D. Song, Y. Liu and N. Wang, Journal of Power Sources, 2018, 379, 350–361.

22 L. Hao, J. Ning, B. Luo, B. Wang, Y. Zhang, Z. Tang, J. Yang, A. Thomas and L. Zhi, Journal of the American Chemical Society, 2015, 137, 219–225.